Biophysical Journal, Volume *121*

Supplemental information

Nucleation causes an actin network to fragment into multiple high-density domains

Aravind Chandrasekaran, Edward Giniger, and Garegin A. Papoian

Nucleation causes an actin network to fragment into multiple high-density domains

Supplementary Information

Aravind Chandrasekaran[1, 2], Edward Giniger[3], Garegin A. Papoian[1, 2*]

[1] Department of Chemistry and Biochemistry, University of Maryland, College Park, Maryland, United States of America

[2] Institute for Physical Science and Technology, University of Maryland, College Park, Maryland, United States of America

[3] National Institutes of Neurological Diseases and Stroke, National Institutes of Health, Bethesda, Maryland, United States of America

*** Contact: gpapoian@umd.edu**

Supplementary Table

Parameter	Symbol	Value	Reference
Geometric parameters			
Compartment size	L_{comp}	500nm	(1)
Number of compartments in each dimension	Nx,Ny,Nz	4,4,15	-
Length of a cylinder	L_{cyl}	40 subunits (108nm)	-
Binding sites per cylinder	$N_{b,sites}$	4	-
Minifilament binding distance	$d_{NMII,bind}$	175-225nm	(1)
α-actinin binding distance	$d_{\alpha,bind}$	30-40nm	(1)
Diffusion rates			
Actin	$k_{actin,diff}$	$20\mu m^2/s$ [80 s^{-1}]	(1)
α-actinin	$k_{\alpha,diff}$	$k_{actin,diff}/10$	(1)
Myosin minifilament	$k_{NMII,diff}$	$k_{actin,diff}/100$	(1)
Enabled	$k_{Ena,diff}$	$k_{actin,diff}/100$	-
Arp2/3	$k_{Arp,diff}$	$k_{actin,diff}/100$	-
Kinetic rate constants			
Actin polymerization at plus end	$k_{actin\ poly,+}$	11.6 $(\mu M.s)^{-1}$ [0.154s^{-1}]	(2)
Actin **de**polymerization at plus end	$k_{actin\ depoly,+}$	1.3 $(\mu M.s)^{-1}$ [0.017s^{-1}]	(2)
Actin polymerization at minus-end	$k_{actin\ poly,-}$	1.4 s^{-1}	(2)
Actin **de**polymerization at minus end	$k_{actin\ depoly,-}$	0.8 s^{-1}	(2)
α-actinin binding	$k_{\alpha,bind}$	0.7 $(\mu M.s)^{-1}$ [0.009 s^{-1}]	(3)
α-actinin unbinding (F=0pN)	$k_{\alpha,unbind}$	0.3 s^{-1}	(3)
NMII head binding, minifilament binding	$k_{head,bind}$, $k_{MF,\ bind}$	0.2s^{-1}, $k_{head,bind}(N_{min+}N_{max})/2$	(4)
NMII head unbinding (F=0pN)	$k_{head,unbind}$	1.0s^{-1}	**a**

Arp2/3 binding	$k_{Arp,bind}$	$0.0017s^{-1}$	**b**(5)
Arp2/3 unbinding (F=0pN)	$k_{Arp,unbind}$	$0.02s^{-1}$	**c**(6)
Mechanochemical constants			
NMII/α-actinin binding pitch on actin filament	-	27nm	(1)
NMII head step size	d_{step}	6.0nm	**d**(7)(8)
NMII minifilament range of number of heads on each side of bipolar minifilament	N_{min}-N_{max}	$N_t \in [15, 30]$	**e**(9, 10)
NMII minifilament stall force	$F_{NMII,stall}$	300pN for minifilament	**f**
NMII per head unbinding Force	$F_{NMII,\ unbind}$	12.62pN per head	(11)
Tunable parameters	β	2.0	(1) **g**
	α	0.2	(1) **g**
Linker unbinding force	$F_{\alpha,\ unbind}$	17.2pN	(12)
Arp2/3 unbinding force	$F_{B,unbind}$	6pN	(13)
Characteristic force of Brownian ratchet	$F_{ratchet}$	1.5pN	(14)
Mechanical constants			
Actin filament stretching constant	$K_{fil,str}$	100pN/nm	(1)
Actin filament bending energy	ε_{bend}	2690pN.nm	(1)
Cylinder-Cylinder Excluded volume constant	K_{vol}	10^5pN.nm^5	(1)
Myosin cross-bridge stiffness	$K_{NMII,str}$	2.5pN/nm	(8)
α-actinin stiffness	$K_{\alpha,str}$	8pN/nm	(15)
Boundary repulsion energy	$\varepsilon_{boundary}$	$10k_BT$	-
Boundary repulsion screening length	Λ	2.7nm	-
Arp2/3 stretching constant	$K_{branch,str}$	100pN/nm	**h**
Arp2/3 bending constant, equilibrium angle	$\epsilon_{branch,bend}$, θ_o	10pN.nm, 70°	**h**
Arp2/3 bending constant #2, equilibrium angle	$\epsilon_{branch,bend,position}$, θ_o	20pN.nm, 90°	**h**
Arp2/3 dihedral constant	$\eta_{branch,dihedral}$	10pN.nm	**h**
Minimization parameters			
Length of the chemical step	$\delta_{chemistry}$	25ms	-
Force tolerance for mechanical minimization	F_T	10pN	-

Table S1 Table of simulation parameters used in MEDYANv4.1 to simulate dendritic actin networks.

aObtained by assuming a duty ratio of 17%, which is the average of the 11% duty ratio corresponding to NMIIA and 23% duty ratio corresponding to NMIIB.(4)
b Obtained from an ODE model as described in reference.
cBased on ATP actin parent filaments.
dValue chosen is close to the *Dictyostelium* step size of 7.3±0.4nm

e Experimental results suggest the total number of heads in NMIIA- 56(10), 58(9), NMIIB-60(9), and NMIIC-28(9). Here, we use a wide range to account for multiple binding modes of myosin isoforms.
f Considering the myosin-actin cross-bridge stiffness of k_{mhead} = 2.5pN/nm (8), the stall force of a single head F_{head} = $k_{mhead}xd_{step}$=15pN. If 15 heads are bound, the $F_{stall,15}$=225pN, while 30 bound heads result in $F_{stall,30}$=450pN. As our simulations dynamically choose myosin heads at binding, a stall force of about 300pN was chosen.
g α parameter tunes the force sensitivity of myosin walking rate while β tunes the force sensitive number of bound myosin heads. Please refer to Supporting Information, Supplementary Methods for a detailed description of the mathematical models used.
h Branching stretching constant is empirically chosen to restrain the distance between parent and offspring filaments. Bending constant is chosen such that the angle does not deviate from the experimentally observed standard deviation.(16, 17). The second bending potential is used to restrict the angle formed by parent cylinder plus end, binding site on parent cylinder, and offspring cylinder minus end (Figure S10) to 90°. Dihedral angle is empirically chosen to ensure parent and offspring filament binding plane is preserved.

[Arp2/3]	M:A=0.1 vs M:A=0.05	M:A=0.05 vs M:A=0.01
1	1.37×10^{-35}	0.0021
5	7.16×10^{-47}	0.0021
10	4.68×10^{-29}	0.0022
25	2.59×10^{-26}	0.87
50	0.86	1.0

Table S2. Table of p-values resulting from pair-wise Wilcoxon test. Null hypothesis is that the two distribution medians are the same and the alternate hypothesis is that the median number of domains is higher under a higher M:A ratio.

Supplementary Figures

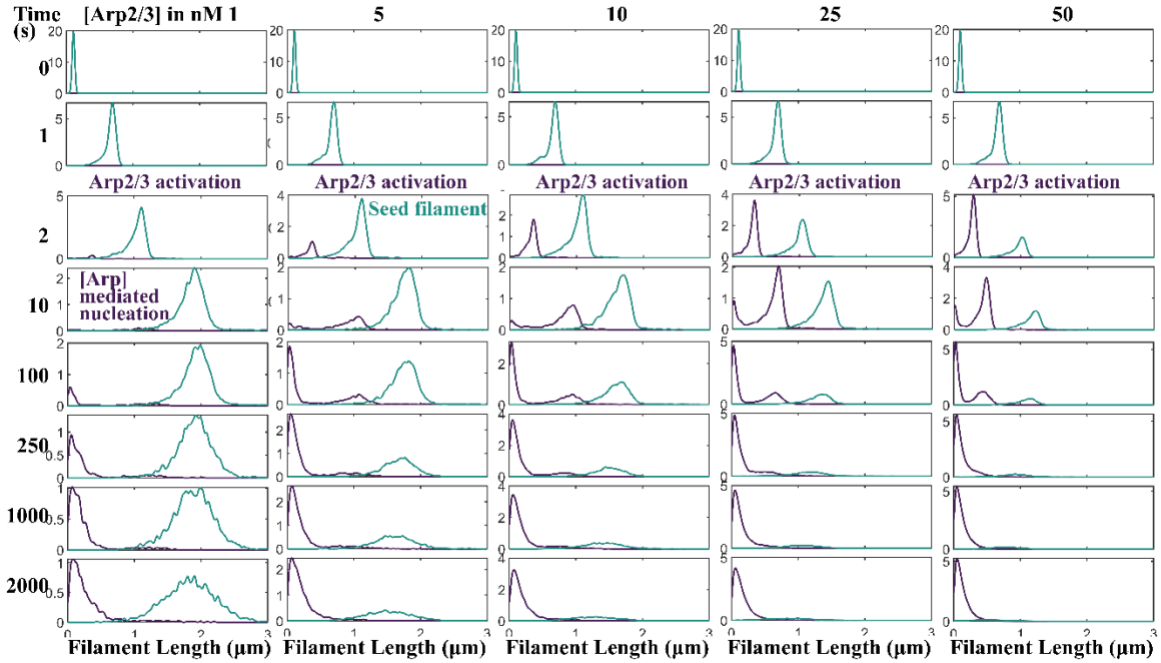

Figure S1 Arp2/3 nucleated filaments reach sub-micron length scales. Filament length distributions are shown at different time points (down each column) of the MEDYAN-generated trajectories at various Arp2/3 concentrations (left to right in each row). Arp2/3 concentrations are mentioned on the top, while simulation time in seconds is mentioned to the left of the figure. Arp2/3 activation at 1s is also shown. At any given Arp2/3 concentration and time (in other words, in any given panel), the length distribution of filaments extended from initial seeds is shown in green, while length distributions of Arp2/3 nucleated filaments are shown in purple.

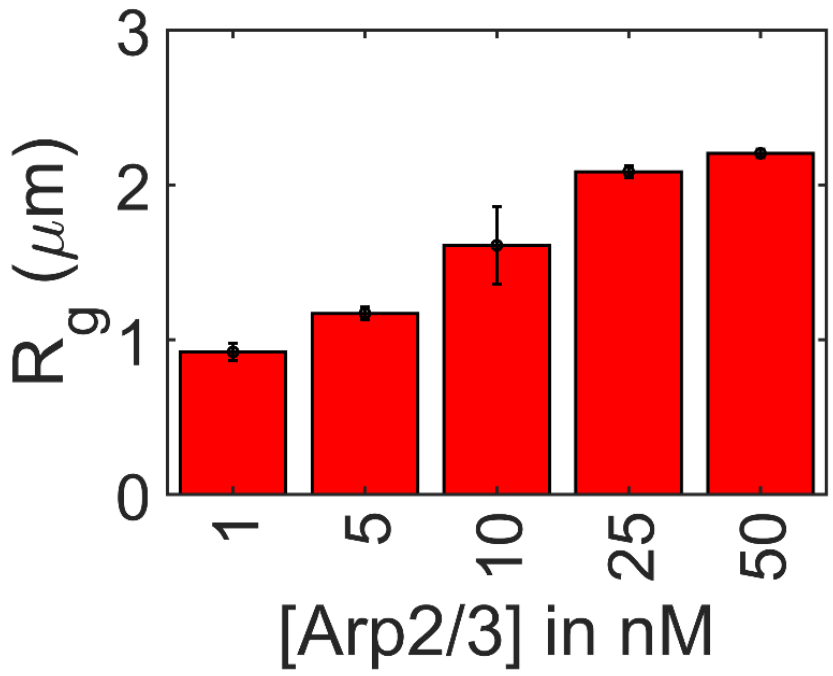

Figure S2. Radius of gyration of F-actin networks at various Arp2/3 concentrations. Mean and standard deviation of network radius of gyration from the last 500s of trajectories are shown at various Arp2/3 concentrations. We see that the network-level configurations of filamentous actin has reached steady-state. Last 500s of six replicates per [Arp2/3].

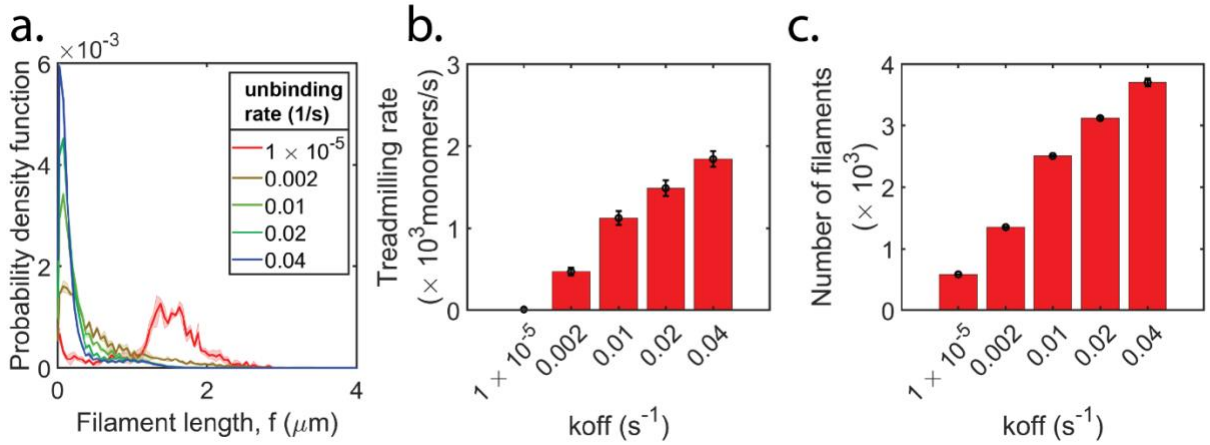

Figure S3. Variation of Arp2/3 unbinding rate shows the role of Arp2/3 residence time at [Arp2/3]=25nM. a) Mean (solid line) and standard deviation (shaded area) of filament length distribution is shown colored by Arp2/3 unbinding rate as shown in the legend. b. The mean treadmilling rate of network is shown at various Arp2/3 unbinding rates. Error bars represent standard deviation. c. The mean total number of filaments in the later part of the simulation is shown as a bar graph for various Arp2/3 unbinding rates. Error bars represent standard deviation. a-c. Data from the last 500s of 3 replicates, sampling frequency=5s.

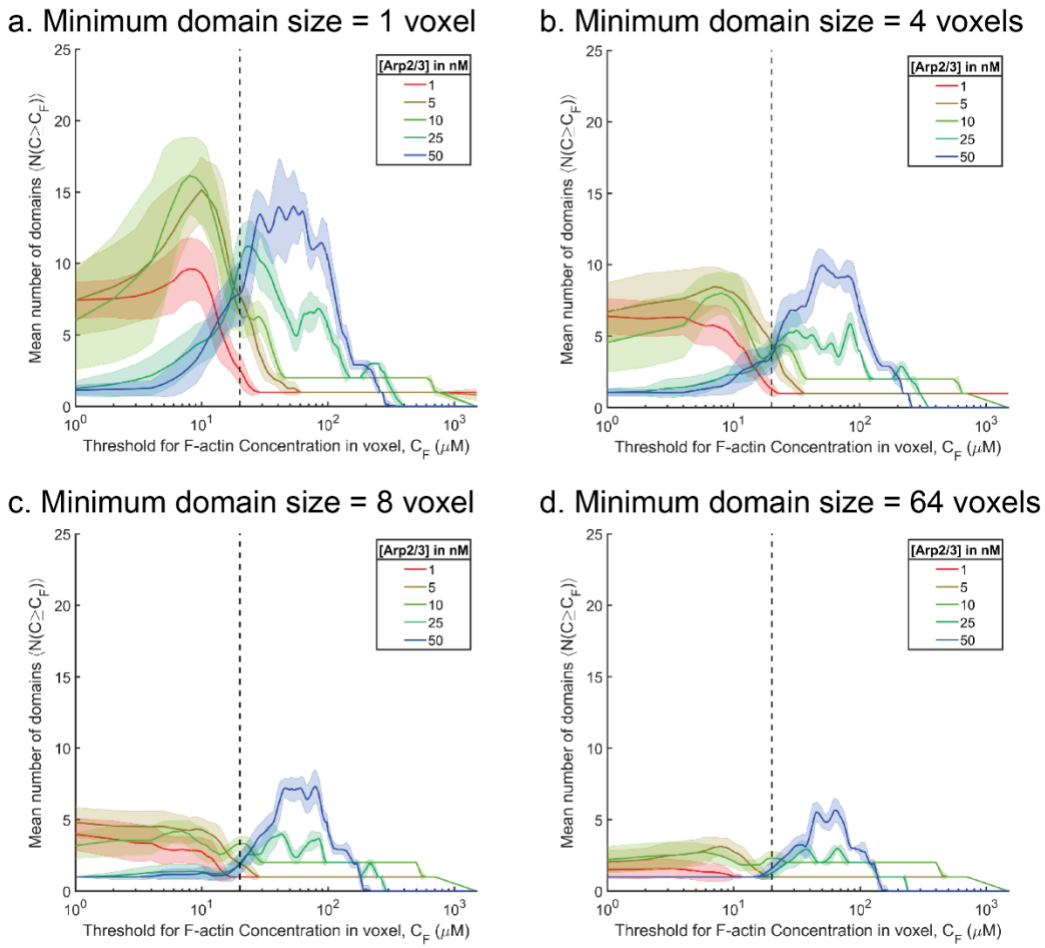

Figure S4. Domain volume threshold do not affect the qualitative trends ion number of domains at various Arp2/3 concentrations. a-d) The number of domains found in last 100s of six trajectories at various Arp2/3 concentrations (shown in legend) are shown. Solid line and shaded area represent mean and standard deviation. Dotted vertical line corresponds to bulk concentration of 20μM.

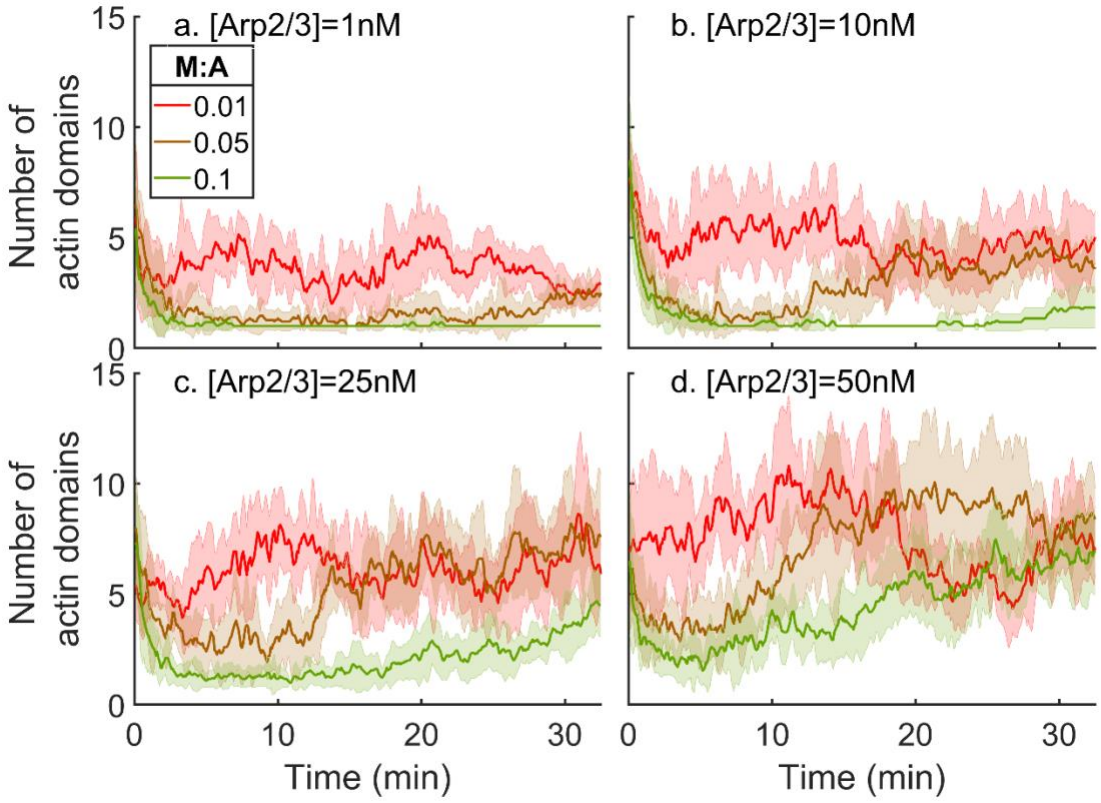

Figure S5. Influence of myosin in contractile dynamics of a dendritic network. a) Plot shows the number of domains in the actin density field obtained at a threshold concentration of 40μM at a) 1nM, b) 10nM, c) 25nM, and d) 50nM Arp2/3 concentration under three different myosin concentrations. Myosin mole ratios are mentioned in the legend. The solid line represents the mean, and the shaded area represents the standard deviation in the number of actin domains.

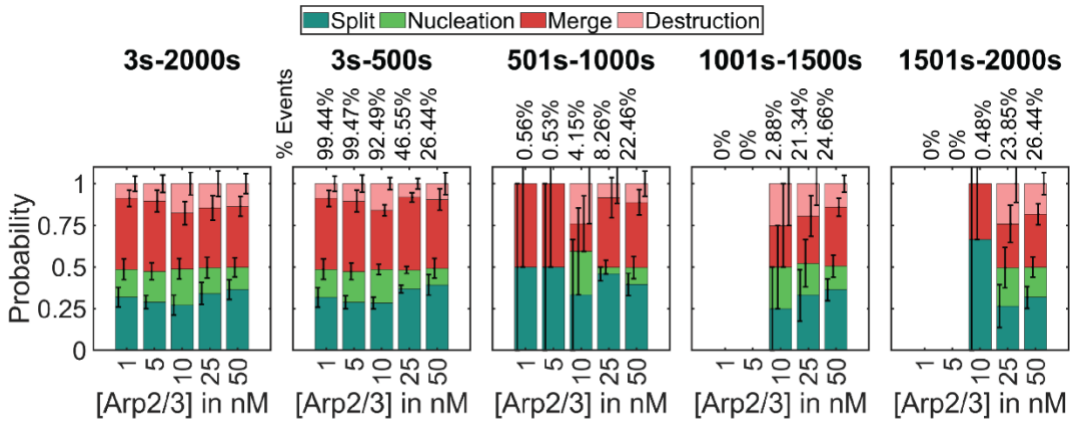

Figure S6. Distribution of different mechanisms that affect the number of high-density actin domains. Pie charts show the percentage of events that lead to birth or loss of domains. Each panel shows the probability of domain split, nucleation, merge and destruction processes along with the standard deviation across trajectories as Arp2/3 concentration is varies along timescales mentioned on the top. Under Arp2/3 concentrations of 1, and 5nM, most of the birth/death events occur in the initial 500s of the trajectories hence we see large standard deviations at later time ranges.

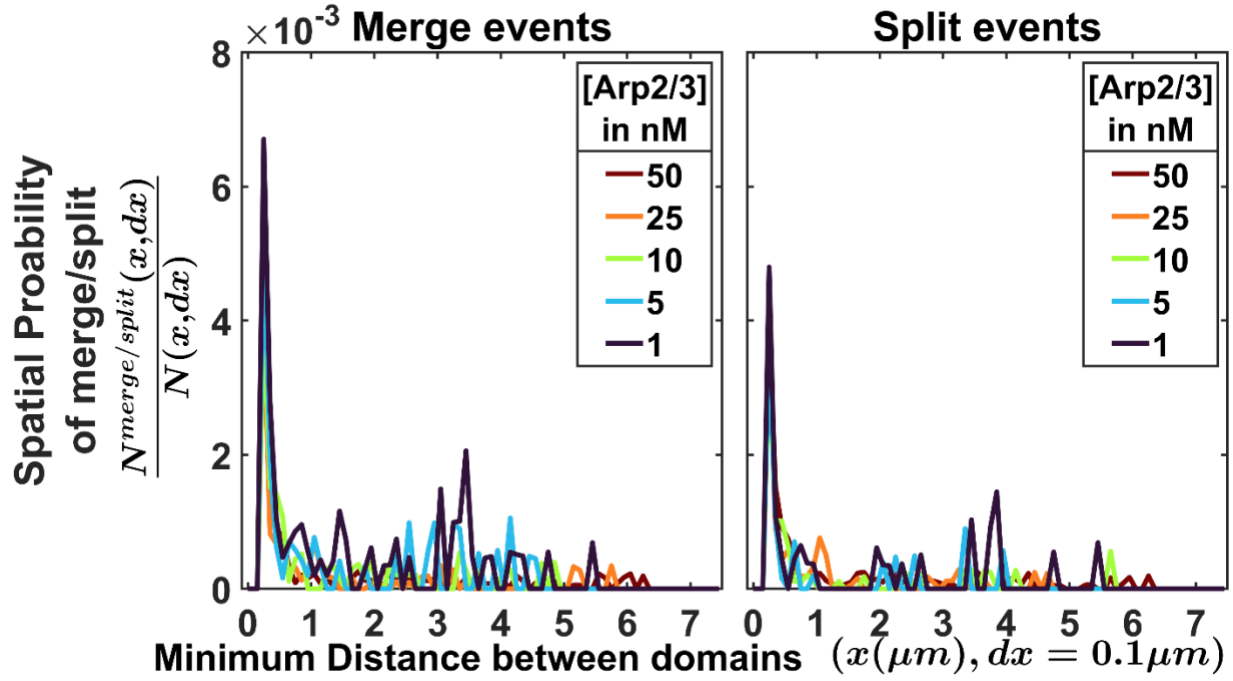

Figure S7. High-density domains are relatively weakly coupled to one another. Probabilities of split and merge events are shown as a function of distance from all time points (six replicates, sampling frequency=1s) in the trajectories. Profiles are colored according to Arp2/3 concentration shown in the legend.

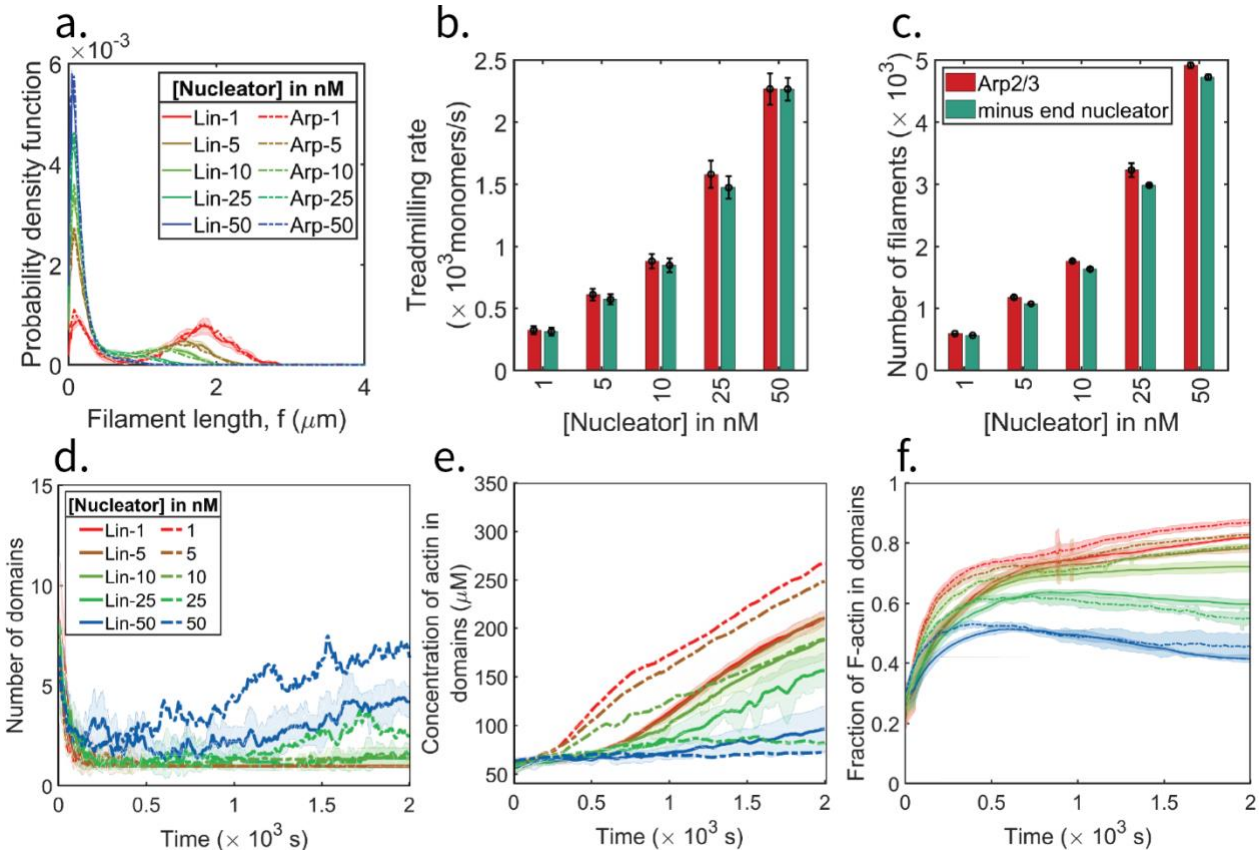

Figure S8. Linear nucleators with Arp2/3 kinetic parameters reproduces fragmentation patterns. a. Mean (solid line) and standard deviation (shaded area) of filament length distributions corresponding to trajectories with linear minus end nucleators are shown. The mean (dashed line) filament length distributions corresponding to various [Arp2/3] are also overlaid showing that both nucleators result in similar filament length distributions. Profiles are colored by nucleator concentration as shown in legend. b. Treadmilling rate from trajectories at various [Arp2/3] (red) and linear minus end nucleators (green) are shown. Error bars represent standard deviation. c. Number of filaments at the end of the simulation at various [Arp2/3] (red) and linear minus end nucleators (green) are shown. Error bars represent standard deviation. a-c. Data from the last 500s of all replicates (linear nucleators = 5, Arp2/3 = 6) was used to generate plots. Data suggests both Arp2/3 and linear minus end nucleator results in networks with similar filament length, treadmilling rate, and total number of filaments. Using 40 μM density threshold, we find the high-actin density domains in the density field. d-f. Profile line patterns and colors correspond to the nucleator type and nucleators concentration respectively as shown in the legend in panel d. d. The mean (solid line) and standard deviation (shaded area) in number of domains identified in trajectories with varying concentration of minus end nucleators is shown as a time profile. Time profiles of mean (dotted line) time profiles of number of domains in trajectories at various [Arp2/3] are also overlaid. e. The concentration of actin in the high-density actin domains from trajectories at various minus end nucleators concentrations are plotted as a time series with mean (solid) line and standard deviation (shaded area). Time profiles of mean (dotted line) actin domain concentration in trajectories with varying [Arp2/3] are also overlaid. f. The fraction of total actin in the high-density domains is plotted as time series showing mean (solid line) and standard deviation (shaded area) corresponding to trajectories at various minus end nucleators concentration. Mean time profiles (dotted line) of actin fraction computed in trajectories at varying [Arp2/3] is also overlaid.

Supplementary Results

The dynamic evolution of actin domains is independent of threshold actin concentration

To ensure that the domain architecture observed in the actin density fields at 40μM threshold concentration is not limited by choice of threshold concentration, we also studied the actin dynamics at 20μM and 30μM thresholds (Figure S9). We see that while the threshold concentration affects the number of high-density actin domains observed, it does not drastically alter the dynamics of actin domains. Thus, our observations reported in the main text are robust to the choice of F-actin concentration. It is worth noting that extremely high threshold concentrations will result in a different picture of actin organization (Figure 2B) but will be a misleading picture as it will include only a tiny fraction of total actin in the network (Figure 2C).

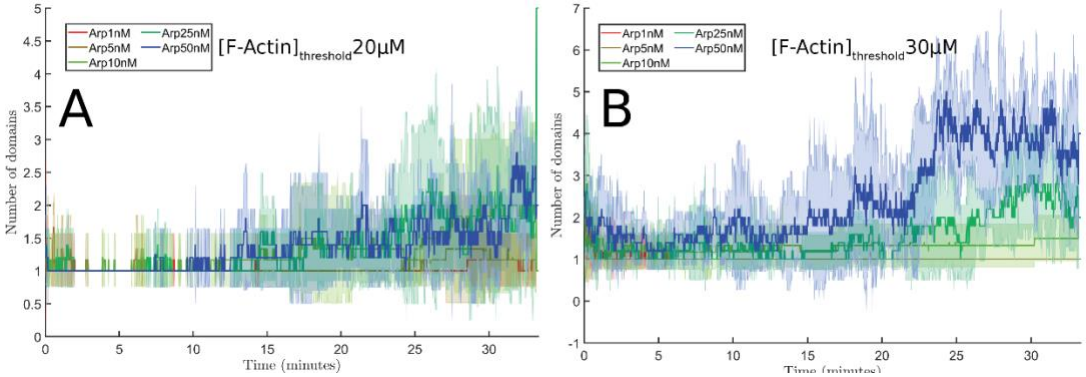

Figure S9. Arp2/3 dependent actin organization is independent of threshold concentration. The time profile of the number of high-density actin domains found by varying Arp2/3 concentration is shown. High-density domains were detected at A. 20 μM and 30 μM local actin concentration thresholds. The solid line and shaded area represent mean and standard deviation, respectively (Sampling frequency=1s).

Supplementary Methods

1. Mechanochemical Dynamics of Active Matter (MEDYAN)

MEDYAN (1) is a C++ based software to simulate mechanochemical dynamics of active matter with special implementations to enable the simulation of filamentous active matter such as actin and microtubules. MEDYAN enables spatially resolved chemical evolution of the reaction network along with physical realism thereby accounting for mechanochemical feedback wherein forces affect reaction chemistry. Here, we outline the key physicochemical paradigms implemented in MEDYAN. In MEDYAN, the filamentous phase and the filament-bound particles are explicitly represented in three-dimensional space while the diffusing pool of molecules are represented as a density field using finite elements.

1.1. Mechanical model of filamentous network

Active filaments are represented as a series of rigid cylinders in three dimensions that resist bending but allow for bending deformations at hinge points. The cylinder length, L_{cyl} (40 monomers, 108nm) is carefully chosen to approximate the curvature of the filaments under contractile forces. Filaments can stretch with stretching constant $K_{fil,str}$ while bending energy, ε_{bend} at hinge points is calculated from the persistence length (L_p) of actin filament as $L_p.k_BT = \varepsilon_{bend}.L_{cyl}$) where k_B represents the Boltzmann constant and temperature T=298K.Additionally, any two cylinders are prevented from overlapping through a cylinder-cylinder excluded volume potential (18). Thus, the mechanical energy of each filament represented by N points in coordinate space is given by the following terms.

$$E_{fil,str} = \sum_{i=1}^{N-1} K_{fil,str}\left(L_{i,i+1} - L_{cyl}\right)^2,$$

$$E_{fil,bend} = \sum_{i=1}^{N-2} \epsilon_{bend} \cos(\pi - \theta_{i,i+1,i+2}).$$

Here, $L_{i,i+1}$ represents the length of cylinder formed by points i and i+1 and $\theta_{i,i+1,i+2}$ represents the angle between points i, i+1, and i+2.

Excluded volume interaction between two cylinder segments is calculated based on the distance r(s,t) between any two points on the cylinder denoted by parameters s and t.

$$E_{fil,vol} = \mathrm{K_{vol}} \int_0^1 \int_0^1 r(s,t)^{-4} ds dt.$$

A more detailed discussion on the excluded volume constant and the physical implication of the functional form can be found here (18).

1.2. Mechanical model of crosslinkers and motor proteins

In MEDYAN, upon a crosslinker/motor binding event, the binding sites are coupled by an elastic spring. This energetic coupling constants for crosslinkers and myosins are given by $K_{\alpha,str}$ and $K_{NMII,str}$ respectively. In this study, motor proteins are represented as NMIIA minifilaments which are small ensembles of non-processive, bipedal proteins. The mechanochemical properties and the stochastic dynamics of minifilaments are represented by the parallel cluster model.(11) Upon minifilament binding, the total number of myosin heads (N_t) is randomly assigned (between 15 and 30 in this study). The stretching constant of the minifilament is assumed to scale linearly with the number of heads as $K_{MF} = K_{NMII,str}.N_t$. Consider two actin filaments that are bound by either a crosslinker or myosin and the binding sites are separated by a distance, L. The mechanical energy due to crosslinker and minifilament coupling are given by,

$$E_{\alpha,str} = K_{\alpha,str}(L - l_0^{\alpha})^2,$$

$$E_{MF,str} = K_{MF,str}(L - l_0^{MF})^2$$

Here, l_0^{α} and l_0^{MF} represent the separation of binding sites at binding.

Mechanical representation of branch points

In MEDYAN, Arp2/3-driven dendritic nucleation leads to the formation of an offspring filament at 70^o with respect to the parent filament. The bound Arp2/3 molecule is represented through a set of interaction potentials that penalize stretching, bending, and dihedral displacements. Figure S10 shows an illustration of the stretching, two bending and one dihedral potentials and the geometric consequences of each.

$$E_{branch,str} = K_{branch,str}(L - L_o)^2,$$

$$E_{branch,bend} = \epsilon_{branch,bend}\cos(\theta - \theta_0),$$

$$E_{branch,dihedral} = \eta_{branch,dihedral}\cos(\overrightarrow{n1},\overrightarrow{n2}).$$

Here, L represents the distance between binding site on the parent filament and the minus-end of the offspring filament (L_o=6nm). For the primary bending potential, θ represents the angle between parent filament and offspring filament ($\theta_0 = 70^o$). For the secondary bending potential, θ represents the angle formed by plus-end of parent cylinder, the binding site on parent cylinder, and the minus end of offspring cylinder ($\theta_0 = 90^o$). $\overrightarrow{n1}$, and $\overrightarrow{n2}$ represent normal of planes as illustrated in Figure S10.

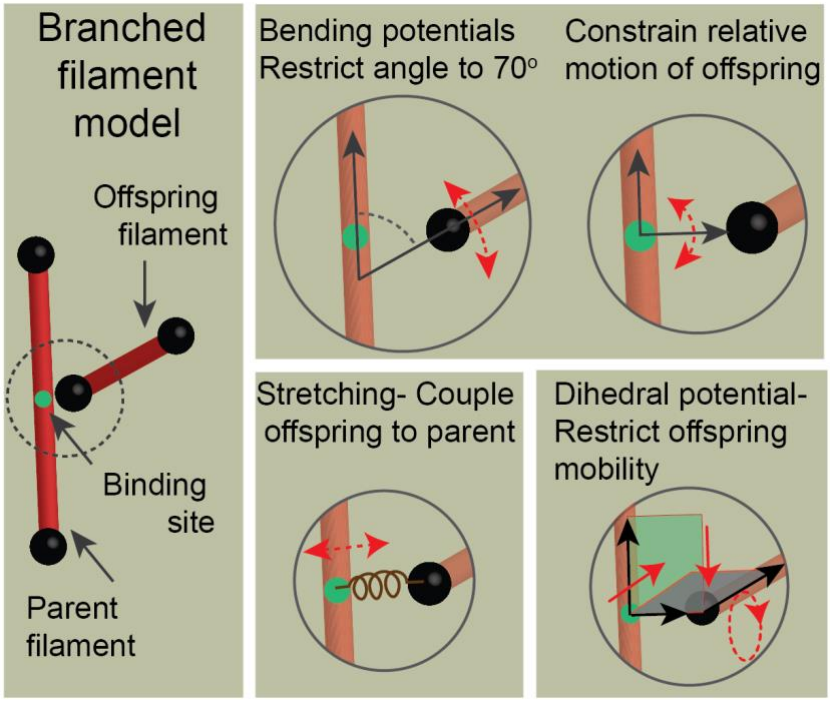

Figure S10. Mechanical energy potentials to represent dendritic branching. Parent and offspring filament segments are shown with cylinder endpoints shown as black spheres. The binding site on the parent filament is shown in green. Panels show various energetic potentials considered and the red dotted arrow represents the corresponding degree of freedom that is restricted.

1.3. Chemical reactions considered

We define the following chemical species in our reaction network.

Chemical species	**Represents**
AD	Diffusing Actin (G-actin)
FA	Filamentous Actin
PE	Plus End
ME	Minus End
MEX	Chemically inactive Minus End
BD	Diffusing brancher
MD	Diffusing myosin minifilament
LD	Diffusing crosslinker
BA	Brancher adhered filamnet end
MA	Filament adhered motor minifilament
LA	Filament adhered linker
FAF	F-actin free of any binding molecule
FAO	F-actin occupied by a binding molecule (M-motor, L-linker)

Table 3: Table of chemical species considered in the rection networks analyzed in this study.
The following chemical reactions have been considered.

$$PE + AD \underset{k^{+}_{actin,depoly}}{\overset{k^{+}_{actin,poly}}{\rightleftharpoons}} FA + PE$$

$$ME + AD \underset{k^{-}_{actin,depoly}}{\overset{k^{-}_{actin,poly}}{\rightleftharpoons}} FA + ME$$

$$BD + AD + FAF \xrightarrow{k_{Arp,bind}} FAO.BA.MEX$$

$$FAO.BA.MEX \xrightarrow{k_{Arp,unbind}} ME + BD + FAF$$

$$MD + 2FAF \underset{k_{MF,unbind}}{\overset{k_{MF,bind}}{\rightleftharpoons}} MA + 2FAOM$$

$$LD + 2FAF \underset{k_{\alpha,unbind}}{\overset{k_{\alpha,bind}}{\rightleftharpoons}} LA + 2FABL$$

$$FAO.M_N + FAF_{N+1} \xrightarrow{k_{MF,walking}} FAF_N + FAO.M_{N+1}$$

Please note that the binding molecule-free F-actin sites should be identified for linker and motor reactions separately such that they are within the respective binding distances ($d_{\alpha,bind}$ and $d_{NMII,bind}$). Additionally, in this study we assume there are four binding sites for actin binding proteins per full length cylinder segment to account for excluded volume interactions between bound molecules.

1.4. Time evolution of reaction network

As seen above, chemical reactions in MEDYAN involve interactions between diffusing molecules and the filamentous phase resulting in a network of reactions that are interdependent on one another. As biological systems often have species at low copy numbers, uniform mixing of all species in the entire reaction volume is physically unreasonable, the reaction volume is divided into sub-volumes (cubes of size 500 nm). The choice of compartment size is guided by the Kuramoto length (19, 20) which represents the reactive mean free length of the fastest reaction in the network (actin plus end polymerization). Further, deterministic techniques have been shown to be inaccurate at low copy numbers and hence it is necessary to consider the stochastic evolution

of such reaction networks. In MEDYAN, we use a computationally optimal version of Gillespie's method (21) called the next reaction method (22). For each reaction, Ri, i [0,N], the execution times τ_μ are randomly calculated based on the propensity ai as $(\tau_\mu = (1/a_\mu) ln (1/r_\mu))$. The reaction with the lowest $\tau_\mu$is executed followed by a dependency update. During the dependency update, all the reactions that share chemical species with Rμ are updated and the corresponding firing rates are recalculated. The series of steps explained above are iteratively repeated to generate the time course of chemical events in a trajectory.

1.5. Mechanochemical considerations

As spatially-resolved Gillespie is essential to capture the mechanochemical realism of cellular active networks, trajectory evolution in MEDYAN involves short bursts of chemical evolution ($\delta_{chemistry}$=25ms in this study) followed by mechanical equilibration to dissipate the stresses accumulated in the system (minimum force in the system F_T=10pN). This separation is based on the underlying assumption that the time scale of chemical evolution is slower than the timescale of mechanical equilibration and that the chemical events do not accumulate excessive stresses that alter the time course of the trajectory.

In addition, experimental evidence suggests that kinetics of specific chemical reactions such as crosslinker/brancher/minifilament unbinding, and minifilament walking are affected by tensions experienced by the chemical species. To account for such variations, we update the chemical rates of such reactions at the end of each minimization cycle using the Bell's formula (23–26) as,

$$k_{\alpha,unbind} = k^0_{\alpha,unbind} \cdot exp\left(\frac{F_{ext}}{F_{\alpha,unbind}}\right),$$

$k_{\alpha,unbind}$ represents the unbinding rate of a crosslinker with a residual tension $F_{ext} = K_{\alpha,str}(L - l_0^{\alpha})$, where L and l_0^{α} represent the current length and equilibrium length of crosslinkers respectively. The zero-force unbinding rate is given by $k_{\alpha,unbind}^0$.

Similarly, the force-sensitive unbinding rate of a brancher is given by,

$$k_{Arp,unbind} = k_{Arp,unbind}^0 \cdot exp\left(\frac{F_{ext}}{F_{B,unbind}}\right),$$

where F_{ext} represents the force on the minus-end of offspring filament resulting from the branching forcefields described above.

The corresponding expression for minifilaments with a total of N_t heads is obtained from parallel cluster model (11). The unbinding rate of minifilament was derived by Erdmann et. al in Ref. (11) and is given by,

$$k_{MF,unbind} = k_{MF,unbind}^0 . \exp\left(-\frac{F_{ext}}{N_b(F_{ext})\mathrm{F_{NMII,unbind}}}\right),$$

where $k_{MF,unbind}^0$ is the zero-force unbinding rate, $F_{ext} = K_{MF,str}(L - l_0^{MF})$, $N_b(F_{ext})$ represents the force-sensitive number of bound heads, and $\mathrm{F_{NMII,unbind}}$ is the characteristic unbinding force per head.

The force-sensitive number of bound heads is given by,

$$N_b(F_{ext}) = \min\left(N_t, \rho N_t + \beta F_{ext}/N_t\right)$$

The zero-force unbinding rate is given by,

$$k_{MF,unbind}^0 \approx \frac{k_{head,bind} N_t}{exp\left(\mathrm{N_t}\log\left(\frac{1}{1-\rho}\right)\right) - 1},$$

where $\rho = k_{head,bind}/(k_{head,bind} + k_{head,unbind})$ represents the duty ratio of individual motors that make the minifilament.

Additionally, the walking rate of motor is also affected by F_{ext} as follows.

$$k_{MF,walk} = k^0_{MF,walk} \frac{\mathrm{F}_{NMII,stall} - \mathrm{F}_{\mathrm{ext}}}{\mathrm{F}_{NMII,stall} + \mathrm{F}_{\mathrm{ext}}/\alpha},$$

given $k^0_{MF,walk}$, the zero-force walking rate, $\mathrm{F}_{NMII,stall}$ the minifilament stall rate, and tunable parameter α. The zero-force walking rate is given by,

$$k^0_{MF,walk} = s k_{head,bind} \frac{1-\rho}{\rho}$$

Here, $s = \mathrm{d}_{\mathrm{step}}\mathrm{N}_{\mathrm{b,sites}}/L_{cyl}$ represents the stepping fraction. This is done to define the walking reaction rate between two binding sites which are separated by $\mathrm{L}_{\mathrm{cyl}}/\mathrm{N}_{\mathrm{b,sites}}$. The tunable parameters α, β, were obtained by fitting the equations to NMII data.

1.6. Force balance for actin-binding proteins

In MEDYAN, the energy minimization step is executed over the points $\{\mathbf{r_i}\}$ that represent the points on the filament. Forces acting on each filament point is given by the gradient, $\mathbf{F}(\mathbf{r_i}) = -\nabla E(\mathbf{r_i})$, where E is the total energy calculated according to the forcefields described above. We employ a variant of the conjugate gradient minimization (27, 28) method known as the Polak–Ribière algorithm (29, 30) to obtain the energy-minimized configuration of the actin network characterized by $|\mathbf{F}(\mathbf{r_i})| \leq \mathrm{F_T}$. During minimization, the forces acting along crosslinkers, and myosins are transformed according to the lever rule to forces that act along the respective filament points. Let us assume that points $\mathbf{r_i}$ and $\mathbf{r_{i+1}}$ along a filament contain a binding site at position $x = |\boldsymbol{r_x} - \boldsymbol{r_i}|/|\boldsymbol{r_i} - \boldsymbol{r_{i+1}}|$ with an actin-binding protein (crosslinker, or myosin). As ABPs are bound two such binding sites, one site experiences a force $F_x = k(l - l_0^{\alpha})$, while the other experiences $-F_x$. As a result, the force F_x is split among filament points as, $F_i = F_x(1-x)$ and $F_{i+1} = F_x.x$.

1.7. Boundary conditions

As the reaction volume is divided into cubic sub-volumes, sub-volumes that are close to the curved surface are partly within and outside the reaction volume. Hence, we make the following modifications to faithfully capture the cylindrical boundary conditions as shown in Figure S11.

1. The diffusion rate between compartments that intersect the boundary surface is scaled by the available interfacial area.
2. The mesoscopic rate constants (c_μ) of reactions are obtained from deterministic rate constants $(k_{\mu)}$ by scaling them based on the volume enclosed within the boundary surface, V_r as follows,

$$c_\mu = k_\mu \left(\frac{V_r}{N_A}\right)^{n-1}$$

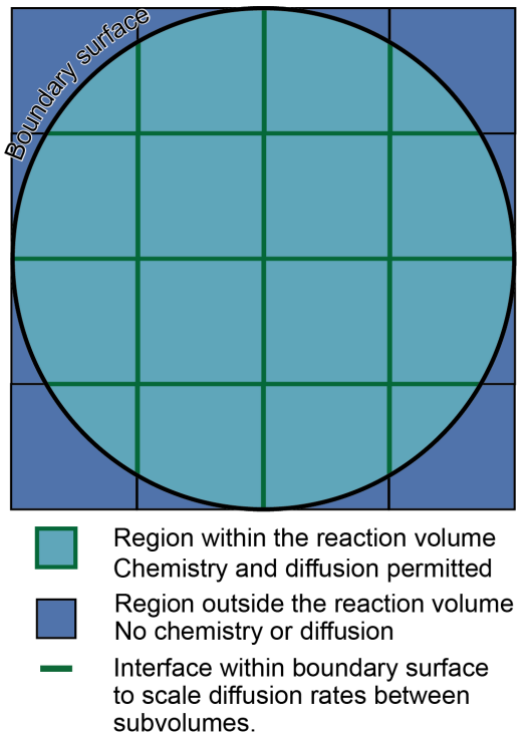

Figure S11. Cartoon of reaction volume cross-section to illustrate chemical boundary conditions. Cartoon shows square sub-volume cross-section along with the boundary surface. Regions outside the reaction volume are shown in dark blue while the regions within the reaction volume are shown in light blue. The interface lengths shown in green are relevant to scale diffusion rates between two compartments.

Diffusion rates of compartments that intersect the boundary layer are scaled in proportion to the interface area enclosed within the sub-volume.

MEDYAN simulations consider enclosed reaction volumes with repulsive boundary conditions. The repulsive energy of the boundary of a filament tip at distance d from the boundary is given by,

$$U_i^{boundary} = \varepsilon_{boundary} e^{-d/\lambda}$$

In addition, Brownian ratchet considerations have also been implemented to ensure that the polymerization rates of free ends reduce as the filament gets closer to the boundary(31).

2. Estimation of drift and diffusion from domain count time-series data

To understand this, we modeled the time series of domain counts from the trajectories at high Arp2/3 concentrations as a stochastic Ito process given by,

$$dN = A(N,t)dt + B(N,t)dW \quad (1)$$

where the number of clusters at time t (N) depends on effective drift term (A) and diffusion coefficient (B). We estimated the effective drift and diffusive terms numerically as,

$$A(n,t) = \lim_{\Delta t \to 0} \frac{\langle N(t+\Delta t) - n \rangle}{\Delta t}\Big|_{N(t)=n} \quad (2)$$

$$B^2(n,t) = \lim_{\Delta t \to 0} \frac{\langle [N(t+\Delta t) - n]^2 \rangle}{\Delta t}\Big|_{N(t)=n} \quad (3)$$

Parameters A and B were estimated at different N(t) values for Δt=1s.

As the above definition of diffusion coefficient still carries the influence of drift(32), we chose to calculate the drift-corrected diffusion coefficient given by,

$$C^2(n,t) = \lim_{\Delta t \to 0} \frac{\langle [N(t+\Delta t) - n - A(n,t)\Delta t]^2 \rangle}{\Delta t}\Big|_{N(t)=n} \quad (4)$$

References

1. Popov, K., J. Komianos, and G.A. Papoian. 2016. MEDYAN : Mechanochemical Simulations of Contraction and Polarity Alignment in Actomyosin Networks. *PLoS Comput. Biol.* 12:e1004877.
2. Fujiwara, I., D. Vavylonis, and T.D. Pollard. 2007. Polymerization kinetics of ADP- and ADP-Pi-actin determined by fluorescence microscopy. *Proc. Natl. Acad. Sci.* 104:8827–8832.
3. Wachsstock, D.H., W.H. Schwartz, and T.D. Pollard. 1993. Affinity of alpha-actinin for actin determines the structure and mechanical properties of actin filament gels. *Biophys. J.* 65:205–14.
4. Kovács, M., F. Wang, A. Hu, Y. Zhang, and J.R. Sellers. 2003. Functional divergence of human cytoplasmic myosin II. Kinetic characterization of the non-muscle IIA isoform. *J. Biol. Chem.* 278:38132–38140.
5. Chandrasekaran, A., A. Clarke, P. Mcqueen, H.Y. Fang, G.A. Papoian, and E. Giniger. 2021. Computational simulations reveal that Abl activity controls cohesiveness of actin networks in growth cones. *bioRxiv doi 10.1101/2021.11.01.466771*. (preprint posted November 2, 2021).
6. Mahaffy, R.E., and T.D. Pollard. 2006. Kinetics of the formation and dissociation of actin filament branches mediated by Arp2/3 complex. *Biophys. J.* 91:3519–3528.
7. Murphy, C.T., R.S. Rock, and J. a Spudich. 2001. A myosin II mutation uncouples ATPase activity from motility and shortens step size. *Nat. Cell Biol.* 3:311–315.
8. Vilfan, A., and T. Duke. 2003. Instabilities in the transient response of muscle. *Biophys. J.* 85:818–827.

9. Billington, N., A. Wang, J. Mao, R.S. Adelstein, and J.R. Sellers. 2013. Characterization of three full-length human nonmuscle myosin II paralogs. *J. Biol. Chem.* 288:33398–33410.

10. Niederman, R., and T.D. Pollard. 1975. Human Platelet Myosin II . In Vitro Assembly and Structure of Myosin Filaments Formation of Platelet Myosin and Myosin Rod Filaments Determination of Platelet Myosin Solubility. *J. Cell Biol.* 67:72–92.

11. Erdmann, T., P.J. Albert, and U.S. Schwarz. 2013. Stochastic dynamics of small ensembles of non-processive molecular motors: The parallel cluster model. *J. Chem. Phys.* 139.

12. Ferrer, J.M., H. Lee, J. Chen, B. Pelz, F. Nakamura, R.D. Kamm, and M.J. Lang. 2008. Measuring molecular rupture forces between single actin filaments and actin-binding proteins. *Proc. Natl. Acad. Sci. U. S. A.* 105:9221–6.

13. Fujiwara, I., S. Suetsugu, S. Uemura, T. Takenawa, and S. Ishiwata. 2002. Visualization and force measurement of branching by Arp2/3 complex and N-WASP in actin filament. *Biochem. Biophys. Res. Commun.* 293:1550–1555.

14. Footer, M.J., J.W.J. Kerssemakers, J.A. Theriot, and M. Dogterom. 2007. Direct measurement of force generation by actin filament polymerization using an optical trap. *Proc. Natl. Acad. Sci.* 104:2181–2186.

15. Didonna, B.A., and A.J. Levine. 2007. Unfolding cross-linkers as rheology regulators in F-actin networks. *Phys. Rev. E - Stat. Nonlinear, Soft Matter Phys.* 75:1–10.

16. Ni, Q., and G.A. Papoian. 2019. Turnover versus Treadmilling in Actin Network Assembly and Remodeling. *Cytoskeleton*. 76:562–570.

17. Mullins, R.D., J.A. Heuser, and T.D. Pollard. 1998. The interaction of Arp2/3 complex

with actin: Nucleation, high affinity pointed end capping, and formation of branching networks of filaments. *Proc. Natl. Acad. Sci.* 95:6181–6186.

18. Floyd, C., A. Chandresekaran, H. Ni, Q. Ni, and G.A. Papoian. 2021. Segmental Lennard-Jones interactions for semi-flexible polymer networks. *Mol. Phys.*

19. Togashi, Y., and K. Kaneko. 2004. Molecular discreteness in reaction-diffusion systems yields steady states not seen in the continuum limit. *Phys. Rev. E - Stat. Physics, Plasmas, Fluids, Relat. Interdiscip. Top.* 70:4.

20. Kuramoto, Y. 1974. Effects of Diffusion on the Fluctuations in Open Chemical Systems. *Progress. Theor. Phys.* 52:711–713.

21. Gillespie, D.T. 1977. Exact stochastic simulation of coupled chemical reactions. *J. Phys. Chem.* 81:2340–2361.

22. Gibson, M.A., and J. Bruck. 2000. Efficient Exact Stochastic Simulation of Chemical Systems with Many Species and Many Channels. *J. Phys. Chem. A.* 104:1876–1889.

23. Bell, G.I. 1978. Models for the Specific Adhesion of Cells to Cells. *Science (80-.).* 200:618–627.

24. Sun, S.X., G. Lan, and E. Atilgan. 2008. Methods in Cell Biology, Chapter 23. Elsevier Inc.

25. Craig, E.M., J. Stricker, M. Gardel, and A. Mogilner. 2015. Model for adhesion clutch explains biphasic relationship between actin flow and traction at the cell leading edge. *Phys. Biol.* 12.

26. Welf, E.S., H.E. Johnson, and J.M. Haugh. 2013. Bidirectional coupling between integrin-mediated signaling and actomyosin mechanics explains matrix-dependent intermittency of leading-edge motility. *Mol. Biol. Cell*. 24:3945–3955.

27. Hager, W.W.W.W., and H. Zhang. 2006. A Survey of Nonlinear Conjugate Gradient Methods. *Pacific J. Optim.* 2:35–58.

28. B. J. Jaidhan, P.S.R.& A.A. 2014. Energy Minimization and Conformation Analysis of Molecules Using Conjugate Gradient Method. *IMPACT Int. J. Res. Eng. Technol. (IMPACT IJRET)*. 2:111–116.

29. Dixon, L.C.W. 1992. Generalized Polak-Ribi re Algorithm. 75:345–354.

30. Touati-Ahmed, D., and C. Storey. 1990. Efficient hybrid conjugate gradient techniques. *J. Optim. Theory Appl.* 64:379–397.

31. Peskin, C.S., G.M. Odell, and G.F. Oster. 1993. Cellular motions and thermal fluctuations: the Brownian ratchet. *Biophys. J.*

32. Devlin, J., D. Husmeier, and J.A. Mackenzie. 2019. Optimal estimation of drift and diffusion coefficients in the presence of static localization error. *Phys. Rev. E*. 100:0–3.